Subannual, Seasonal, and Interannual Variability of the North Atlantic Meridional Overturning Circulation

JOËL J.-M. HIRSCHI, PETER D. KILLWORTH, AND JEFFREY R. BLUNDELL

National Oceanography Centre, Southampton, Southampton, United Kingdom

(Manuscript received 30 March 2006, in final form 14 August 2006)

ABSTRACT

An eddy-permitting numerical ocean model is used to investigate the variability of the meridional overturning circulation (MOC). Both wind stress and fluctuations of the seawater density contribute to MOC changes on subannual and seasonal time scales, whereas the interannual variability mainly reflects changes in the density field. Even on subannual and seasonal time scales, a significant fraction of the total MOC variability is due to changes of the density field in the upper 1000 m of the ocean. These changes reflect perturbations of the isopycnal structure that travel westward as Rossby waves. Because of a temporally changing phase difference between the eastern and western boundaries, the Rossby waves affect the MOC by modifying the basinwide east–west density gradient. Both the numerical model used in this study and calculations based on Rossby wave theory suggest that this effect can account for an MOC variability of several Sverdrups ($Sv \equiv 10^6\ m^3\ s^{-1}$). These results have implications for the interpretation of variability signals inferred from hydrographic sections and might contribute to the understanding of the results obtained from the Rapid Climate Change (RAPID) monitoring array deployed at 26°N in the North Atlantic Ocean.

1. Introduction

The variability of the Atlantic Ocean meridional overturning circulation (MOC) is a key element in understanding the past, present, and future climate. Currently the Atlantic MOC transports about 1 PW (10^{15} W) of heat northward (Trenberth and Caron 2001), thus contributing to Europe's characteristic mild climate. Paleoclimatic archives suggest that in the past the MOC has undergone large changes (Heinrich 1988; Dansgaard et al. 1993). During the last ice age abrupt changes associated with temperature variations of more than 10°C over Greenland were not uncommon (e.g., Lang et al. 1999), and one plausible mechanism is a changing strength of the MOC (e.g., Broecker et al. 1992). Early model results suggest that the MOC can operate in more than one mode (e.g., Stommel 1961; Marotzke and Willebrand 1991), and the existence of possible thresholds between different MOC states is a subject of ongoing research (e.g., Tziperman 1997; Zanna and Tziperman 2005). A shutdown of the MOC is likely to lead to a temperature drop over the North Atlantic area (e.g., Vellinga and Woods 2002). During the last century anthropogenic emissions have raised the levels of greenhouse gases to a level unprecedented during the last 500 kyr (Petit et al. 1999; Siegenthaler et al. 2005), thus raising the question of the future behavior of the MOC. Currently, most model studies agree that increasing levels of carbon dioxide (CO_2) in the atmosphere could be responsible for a weakening of the MOC (Houghton et al. 2001). A recent observation-based study using five hydrographic sections at 25°N indicates that the MOC could have slowed down by as much as 30% since 1957 (Bryden et al. 2005a).

Whether this change is part of an MOC oscillation or a long-term trend is not yet clear. Based on observational data, Polyakov et al. (2005) show the presence of multidecadal variability in the North Atlantic.

Numerical studies indicate that the MOC can vary on subannual to millennial time scales. Wind-driven changes such as those related to Ekman transports can lead to substantial MOC changes on subannual and seasonal time scales (e.g., Willebrand et al. 1980; Schopf 1980; Bryan 1982; Jayne and Marotzke 2001), and recent work by Köhl (2005) suggests that MOC variability on seasonal time scales can be induced by wind-driven upwelling and downwelling at the eastern boundary.

Corresponding author address: Dr. Joël J.-M. Hirschi, National Oceanography Centre, Southampton, European Way, Southampton SO14 3ZH, United Kingdom.
E-mail: jjmh@noc.soton.ac.uk

DOI: 10.1175/JPO3049.1

Several studies have investigated subannual and seasonal MOC variability linked to fluctuations of the meridional transport at the northern boundary of idealized two-layer models. Examples are Kawase (1987), Johnson and Marshall (2002), and Deshayes and Frankignoul (1995) who have shown that in these models Kelvin and Rossby waves generated by high-latitude perturbations can affect the basinwide MOC on time scales of less than 1 yr. While Johnson and Marshall (2002) highlight the combined effect of Kelvin and Rossby waves, Deshayes and Frankignoul (1995) specify the influence of the perturbations along the western boundary (Kelvin waves) versus those in the basin interior (Rossby waves). On interannual to interdecadal time scales the MOC variability is thought to be linked to atmospheric variability patterns, such as the North Atlantic Oscillation (e.g., Delworth et al. 1993; Delworth and Greatbatch 2000; Eden and Greatbatch 2003). MOC variability on centennial to millennial time scales is thought to have occurred during the last ice age as a consequence of iceberg (freshwater) discharges linked to instabilities of the ice sheets that covered large parts of North America and Europe at that time (Ganopolski and Rahmstorf 2001).

From the studies summarized above it emerges that, while the short-term variability (subannual, seasonal, interannual) linked to the wind stress through Ekman transports can be explained relatively well, the understanding of MOC changes due to fluctuations of the large-scale density field (even if they might be linked to the wind stress) is still incomplete. The studies of Baehr et al. (2004) and Hirschi and Marotzke (2007) have shown that even on short time scales a substantial fraction of the total variability is due to changes of the density field. A better understanding of the density-related changes of the ocean circulation on subannual to interannual time scales is a prerequisite for the interpretation of data collected by recently deployed observing systems such as the Natural Environment Research Council (NERC) Rapid Climate Change (RAPID) monitoring array at 26°N in the North Atlantic (Marotzke et al. 2002). Thanks to these systems, new data allowing an estimate of the MOC strength and variability will become available, and one major challenge will be to find the correct interpretation of the inferred variability signals. As in the study of Bryden et al. (2005a) the question whether an observed MOC signal is part of a trend or a temporary oscillation will not be easy to answer. The relatively short time series (the initial deployment period for the RAPID array at 26°N is 5 yr) means that there will be a particular emphasis on short time scales (subannual, seasonal).

The purpose of the present study is to use an eddy-permitting numerical model to investigate what variability signals can be expected for the MOC on subannual, seasonal, and interannual time scales and what the underlying mechanisms are. The main goal is to improve our understanding of processes that are relevant for the correct interpretation of observing systems, such as the RAPID array at 26°. The paper is organized as follows: After a brief description of the numerical model in section 2 we use the method in section 3 to infer the simulated MOC variability described in section 4; section 5 gives a conceptual model based on Rossby wave theory, and a discussion and conclusions are given in sections 6 and 7.

2. Model description

The model used here is a ¼° version of the Ocean Circulation and Climate Advanced Modelling Project (OCCAM) described in Webb (1996) and Marsh et al. (2005a,b). OCCAM is a global general circulation model with realistic topography. The vertical is divided into 66 levels with thicknesses ranging from 5 m at the surface to 207 m for the bottom level. The surface forcing consists of 6-hourly National Centers for Environmental Prediction fluxes for wind, heat, and $E - P$ (Kalnay et al. 1996). For the sea surface salinity there is an additional restoring term to monthly surface salinity values of Levitus et al. (1998). The model simulates the global ocean circulation for the years 1985–2003. In the present study we only use a North Atlantic portion of OCCAM extending from the equator to 70°N. Owing to its relatively high resolution OCCAM is eddy permitting, and the best representation of eddies is achieved at low latitudes where the Rossby radius is large. However, eddies can be simulated reasonably well up to midlatitudes. In the Agulhas region the persistence time of eddies compares well with observations and the results from a 1/12° version of OCCAM (Donners and Drijfhout 2004). The limitations of the ¼° resolution become apparent in the representation of the energy cascade from larger to smaller length scales (e.g., breakup of eddies into cyclonic–anticyclonic pairs), which cannot be resolved.

3. Method

To distinguish between MOC variability due to the zonal wind stress and changes in density we consider the Ekman- and density-driven MOC components separately. These components are computed following the same approach as in Hirschi and Marotzke (2007). The Ekman component ψ_{Ek} is defined as

$$\psi_{\mathrm{Ek}}(z') = \int_{x_w}^{x_e} dx \int_{-H(x)}^{z'} dz[\upsilon_{\mathrm{Ek}}(x, z) - \bar{\upsilon}_{\mathrm{Ek}}(x)], \tag{1}$$

where

$$\upsilon_{\mathrm{Ek}} = -\frac{1}{\rho^* f L \Delta z} \int_{x_w}^{x_e} \tau^x \, dx \quad \text{and}$$

$$\bar{\upsilon}_{\mathrm{Ek}} = -\frac{1}{\rho^* f A} \int_{x_w}^{x_e} \tau^x \, dx, \tag{2}$$

and where τ^x, ρ^*, f, L, H, x_e, x_w, Δz, and A are the zonal wind stress, a reference density, the Coriolis parameter, the basin width, its depth, the eastern and western margins, an assumed thickness for the Ekman layer, and the cross-sectional area, respectively. The velocity in the Ekman layer is υ_{Ek} and $\bar{\upsilon}_{\mathrm{Ek}}$ is a depth-independent flow compensating the Ekman transport (Jayne and Marotzke 2001).

The density contribution ψ_{tw} is based on the thermal wind approach, and as in Baehr et al. (2004) the full density field ρ is used:

$$\psi_{\mathrm{tw}} = \int_{x_w}^{x_e} dx \int_{-H(x)}^{z'} dz \left(\int_{-H}^{z'} \upsilon_z \, dz - \bar{\upsilon} \right), \tag{3}$$

where the shear is obtained through the thermal wind balance

$$f\upsilon_z = -\frac{g}{\rho^*} \rho_x, \tag{4}$$

and where $\bar{\upsilon}$ is a spatially constant velocity correction that ensures the mass balance for ψ_{tw}. The subscripts x and z denote zonal and vertical differentiation, respectively. As shown by Hirschi and Marotzke (2007), the sum of ψ_{Ek} and ψ_{tw} largely captures the spatial and temporal structure of the MOC in the North Atlantic. Shortcomings occur at locations where large meridional velocities are found over sloping topography. In this case the barotropic flow projects onto the MOC, and the sum of the Ekman and thermal wind contributions either over- or underestimates the meridional flow (for details see Hirschi and Marotzke 2007; Baehr et al. 2004).

4. Variability of the meridional flow

In this section the MOC variability occurring in OCCAM from 1985 to 2003 is illustrated for the North Atlantic MOC cell, and a detailed study of the zonal structure of the meridional transport is carried out at latitudes of 10°, 26°, 36°, and 45°N. Apart from 10°N, these latitudes are those where observing systems are currently deployed in the framework of the NERC Rapid Climate Change thematic program (Marotzke et al. 2002).

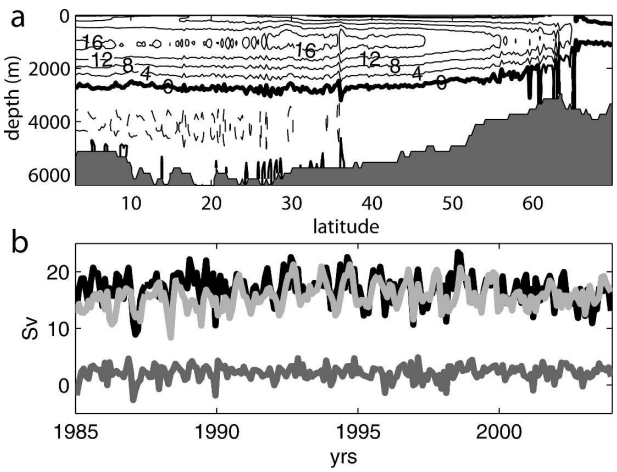

FIG. 1. (a) MOC in OCCAM (average 1985–2003). Units: Sv; the contour interval is 4 Sv. (b) Illustration of variability (monthly averages) at 26°N at a depth of 1100 m for the MOC (black), thermal wind contribution (light gray), and Ekman transport (dark gray). The standard deviations for the thermal wind and Ekman contributions are 2.3 and 1.4 Sv, respectively.

a. Variability of the zonally integrated flow

The temporal average of the North Atlantic MOC shows one cell extending up to 65°N with a maximum value of about 16 Sv (Sv $\equiv 10^6$ m^3 s^{-1}, Fig. 1a). The highest values are reached at 1100-m depth, and the southward return flow is found between 1100 m and 2500 m. The MOC variability reflects changes in both the Ekman and thermal wind contributions ψ_{Ek} and ψ_{tw}, as illustrated for 26°N at 1100-m depth (Fig. 1b). Changes of 5 Sv within a few months are not uncommon for the MOC and ψ_{tw}, whereas a smaller variability is found for ψ_{Ek}.

The standard deviation (std dev) for the period 1985–2003 shows that substantial variability is found for the MOC cell over a large fraction of the North Atlantic (Fig. 2a). The highest values occur south of 15°N where the std dev reaches 4.5 Sv. The highest variability is confined to the surface ocean, with a gradual decrease with depth. North of 15°N the variability is smaller, but nevertheless values of more than 1.5 Sv occur between 15° and 55°N. Unlike the variability farther south, the largest values generally do not occur at the surface.

For the thermal wind component ψ_{tw} the largest variability occurs at around 1000-m depth with maxima between 35° and 30°N and south of 15°N (Fig. 2b). The high values found in the southernmost latitudes are due to limitations of the calculation used for the density

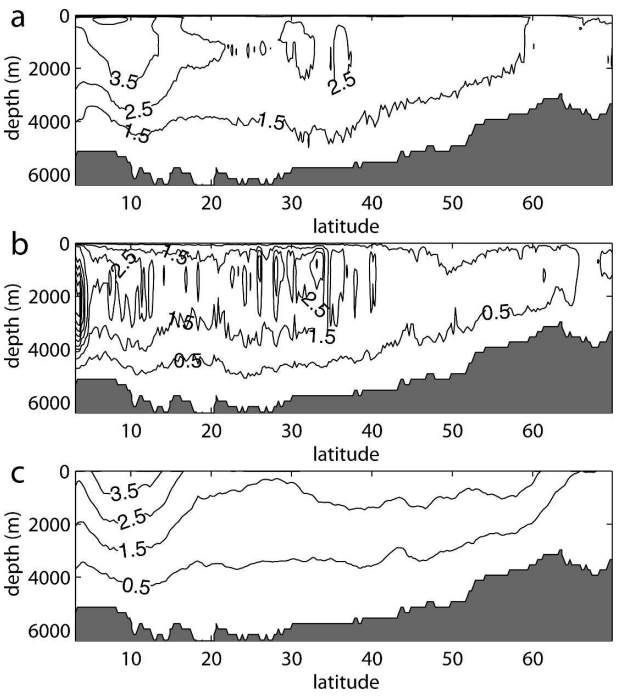

FIG. 2. Standard deviations obtained from monthly averages for the period from 1985 to 2003 for (a) the MOC, (b) the thermal wind (baroclinic) contribution ψ_{tw}, and (c) the Ekman contribution ψ_{Ek}. Units: Sv; the contour interval is 1 Sv.

contributions in near-equatorial regions (Hirschi and Marotzke 2007). For the Ekman contribution ψ_{Ek} (Fig. 2c) the largest variability coincides with the area of high variability south of 15°N for the MOC. The largest values occur at the surface since we assume an Ekman transport in the top layers that is compensated by a depth-independent return flow (Hirschi and Marotzke 2007).

The picture that emerges from Fig. 2 is that the MOC variability is due to a combination of the density and wind contributions. The large variability with maximum values at the surface found south of 15°N reflects the action of the wind, whereas the variability found between 15° and 40°N with maximum values at 1000-m depth is linked to changes in the density field.

b. Time scales

The standard deviation discussed above can be caused by circulation changes occurring on long or short time scales. Therefore, it is useful to split the variability simulated in OCCAM into long- and short-term signals. We decompose the total variability found for the MOC and its components ψ_{tw} and ψ_{Ek} into a subannual (ψ'), a seasonal ($\hat{\psi}$), and an interannual component (ψ^*) according to

$$\psi' = \overline{\psi}_1 - \overline{\psi}_2, \tag{5}$$

$$\hat{\psi} = \overline{\psi}_2 - \overline{\psi}_3, \quad \text{and} \tag{6}$$

$$\psi^* = \overline{\psi}_3 - \overline{\psi}_4, \tag{7}$$

where $\overline{\psi}_1$, $\overline{\psi}_2$, and $\overline{\psi}_3$ are time series that consist of 5-day averages that are filtered with Parzen filter lengths of 1, 5, and 23 months, respectively, and $\overline{\psi}_4$ is the mean value for the years 1985–2003. This decomposition of the variability signals is applied at 10°, 26°, 36°, and 45°N.

The variability in the filtered time series of $\overline{\psi}_1$, $\overline{\psi}_2$, and $\overline{\psi}_3$ for the MOC, ψ_{tw}, and ψ_{Ek} is illustrated in Fig. 3. Table 1 summarizes the variability amplitudes found for the subannual, seasonal, and interannual components ψ', $\hat{\psi}$, and ψ^* according to Eqs. (5)–(7). Except at 45°N, the largest variability contributions are found on subannual and seasonal time scales. At 10°N (Fig. 3a) $\overline{\psi}_1$ indicates a pronounced subannual variability for the MOC and the standard deviation for ψ' is 2.3 Sv. A more regular signal is observed for $\overline{\psi}_2$, which exhibits an annual cycle with maximum values occurring at the end of each year and a minimum at midyear. Peak-to-peak amplitudes are 10 Sv and the standard deviation for $\hat{\psi}$ is 2.9 Sv. The interannual evolution of $\overline{\psi}_3$ shows smaller changes with an std dev of 0.7 Sv for ψ^*. At 26°N (Fig. 3b, top) a large variability is seen on subannual time scales, but the amplitude is slightly smaller (std dev 1.9 Sv for ψ'). On seasonal time scales there is no clear annual signal. Years with a single peak and trough alternate with years where several maxima/minima occur. The amplitude of the seasonal variability is smaller than at 10°N with a standard deviation of 1.3 Sv. The interannual signal is similar in amplitude to that at 10°N, with a standard deviation of 0.8 Sv. At 36°N (Fig. 3c) the subannual signal strength is similar to 26°N, but the seasonal signal is stronger. As at 10° and 26°N, the interannual signal provides the smallest contribution. A different picture is seen at 45°N (Fig. 3d), where the interannual variability provides the largest signal (std dev 1.8 Sv for ψ^*).

At 10°, 26°, and 36°N the subannual and seasonal variability seen for the MOC is reflected in both the thermal wind and the Ekman contributions (Figs. 3a–c, middle and bottom; Table 1). The annual cycle previously described for the MOC at 10°N is seen in the thermal wind as well as in the Ekman transport. Note that the variability of the two components are not in phase: the peaks and troughs of ψ_{Ek} lag those of ψ_{tw} by about 2 months (Fig. 3a). The amplitude of the variability is larger for ψ_{Ek} (std dev 2.3 Sv) than for ψ_{tw} (std dev 1.6 Sv). At 10°N the seasonal variability is linked to the meridional shift of the intertropical convergence

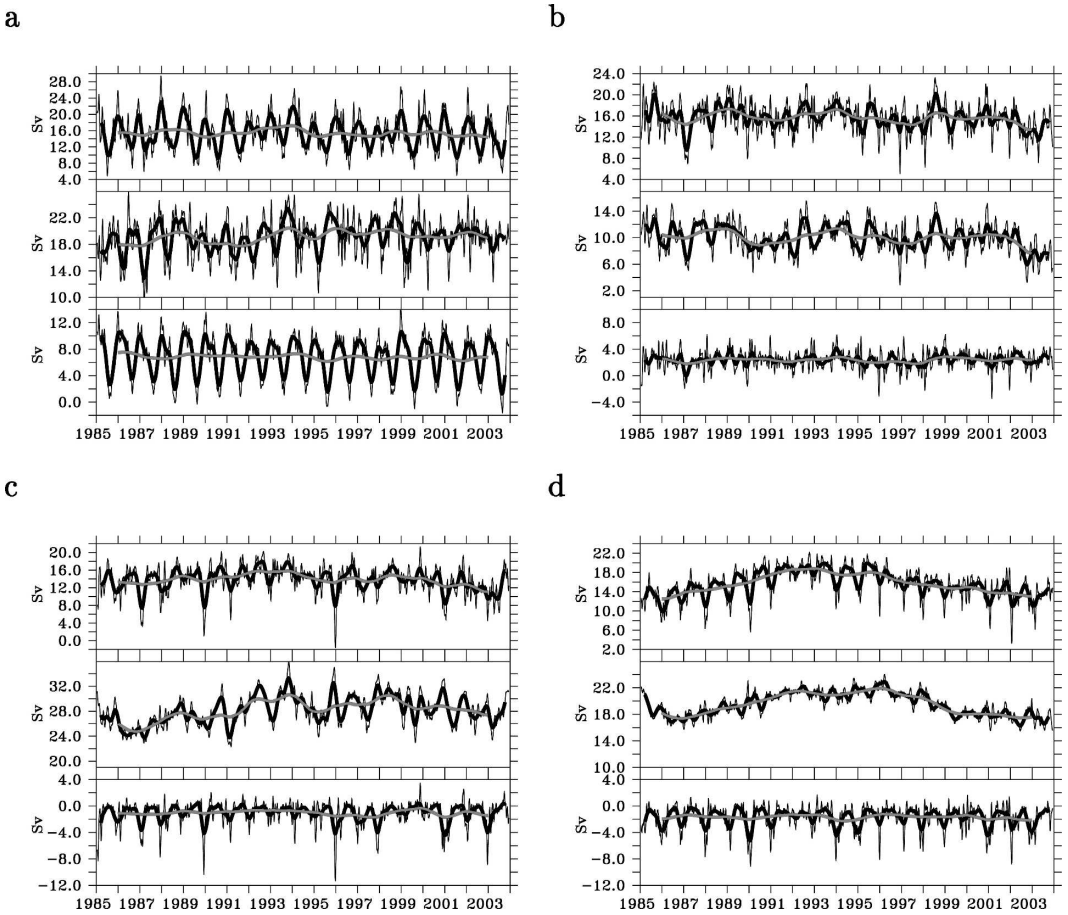

FIG. 3. MOC variability at (a) 10°, (b) 26°, (c) 36°, and (d) 45°N. The time series are smoothed with a Parzen filter of 1 month ($\overline{\psi}_1$, thin black), 5 months ($\overline{\psi}_2$, black), and 24 months ($\overline{\psi}_3$, gray). For each latitude, the values are shown for (top) MOC, (middle), ψ_{tw}, and (bottom) ψ_{Ek}. The values are shown for a depth of 1100 m, and the range is 26 (top panels) and 16 Sv (middle and bottom panels).

zone (ITCZ) and with the associated wind stress changes. At 26° and 36°N, ψ_{tw} dominates the seasonal variability whereas both ψ_{tw} and ψ_{Ek} equally contribute to the subannual signal. At 45°N the main cause of the subannual and seasonal variability is the Ekman transport (Fig. 3d, Table 1). One feature common to all four latitudes is that ψ_{tw} accounts for a large fraction of the interannual variability, whereas only little variability is associated with ψ_{Ek} on these time scales (Fig. 3, Table 1).

An interesting feature illustrated in this section is that high-frequency variability (subannual, seasonal) is due to changes occurring in the density field as well as to the surface wind stress. The strength and pattern of

TABLE 1. Standard deviations for the MOC, the thermal wind contribution ψ_{tw}, and the Ekman contribution ψ_{Ek} at selected latitudes. Values are shown for the total transports as well as for the subannual (ψ'), seasonal ($\hat{\psi}$), and interannual (ψ^*) components for a depth of 1100 m. Units: Sv.

	MOC				ψ_{tw}				ψ_{Ek}			
Latitude (°N)	Total	ψ'	$\hat{\psi}$	ψ^*	Total	ψ'	$\hat{\psi}$	ψ^*	Total	ψ'	$\hat{\psi}$	ψ^*
10	4.4	2.3	2.9	0.7	2.9	1.9	1.6	0.8	3.2	1.1	2.3	0.3
26	2.9	1.9	1.3	0.8	2.3	1.3	1.2	0.8	1.4	1.0	0.5	0.3
36	3.1	1.8	1.6	1.0	2.5	0.9	1.3	1.5	1.8	1.1	0.9	0.3
45	3.1	1.5	1.4	1.8	1.8	0.6	0.5	1.5	1.7	1.1	1.0	0.3

the wind field can vary on short time scales. This can be due to the alternating passage of high and low pressure areas at midlatitudes or seasonal changes such as the trade winds. For the density field it is less obvious what causes such rapid changes. One would rather expect the large-scale density field and the related meridional transports to change on longer time scales (decadal or more) that are typically required to allow the ocean circulation to adjust to changes (e.g., Döscher et al. 1994). In OCCAM changes of more than 5 Sv within a few months are not uncommon (Fig. 3). This suggests that depending on when "measurements" (e.g., a hydrographic section) are undertaken, different states of the MOC might be inferred. If one considers the total variability seen for the baroclinic contribution ψ_{tw} at 26°N (Fig. 3b, middle), measurements taken in early 1987 would yield a baroclinic transport of about 6 Sv. From a repeat section taken in early 1994 one would infer a baroclinic transport of about 12 Sv, indicating an apparent doubling of the MOC during that period. By looking at the complete time series, we see that this is not the case: the baroclinic transport oscillates around a mean value of 10 Sv and there is no obvious trend in the circulation.

c. Zonal structure of the meridional flow

Even if the total baroclinic variability ultimately depends on density differences between the eastern and western margins (Hirschi and Marotzke 2007), the mechanisms causing these differences might be found in the basin interior.

We examine the zonal structure of the density-driven flow by using the cumulative baroclinic transport,

$$\psi_c(x, z) = \int_0^z dz \int_{x_e(z)}^x v' \, dx, \tag{8}$$

where v' is the baroclinic velocity component obtained from the thermal wind relation,

$$v'(z) = \int_z^{-H} v'_z \, dz = -\frac{g}{f\rho^*} \int_z^{-H} \rho_x \, dz \, . \tag{9}$$

The transport is integrated westward starting at the eastern boundary; x_e in Eq. (8) denotes the location of the eastern margin. The transport ψ_c highlights which longitudes contribute most to the variability of the basinwide transport. If the zonal integration in Eq. (8) is extended over the entire basin width, ψ_c is identical to the thermal wind contribution ψ_{tw}.

The standard deviation of ψ_c provides a first idea of where the flow varies most. All four latitudes considered here show a similar pattern, with the largest variability occurring close to the western boundary (Fig. 4).

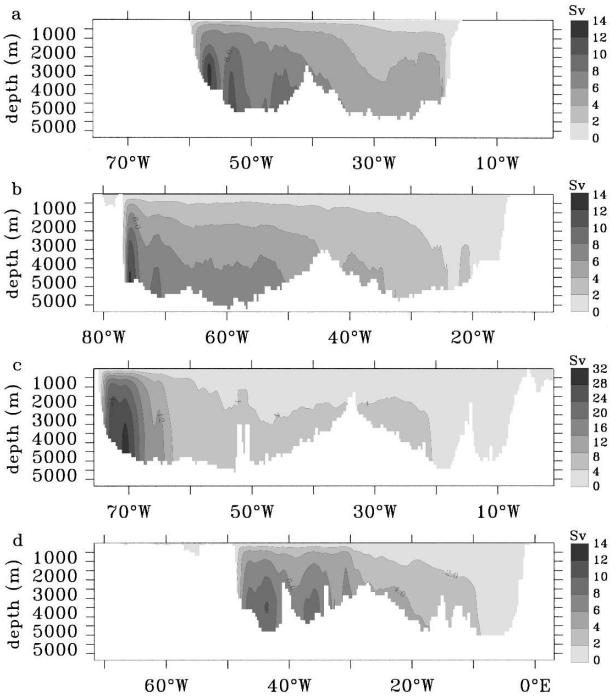

FIG. 4. Standard deviation for the cumulative baroclinic transport (Sv) at (a) 10°, (b) 26°, (c) 36°, and (d) 45°N. The contour interval is 2 Sv in (a), (b), and (d) and 4 Sv in (c).

Relatively little variability is found east of the Mid-Atlantic Ridge. The maximum values of 28 Sv (36°N), 14 Sv (26° and 45°N), and 10 Sv (10°N) are found close to the western margin. The maximum standard deviations are higher than the values found for the basinwide integral (Fig. 4, Table 1) and there is a sharp decrease in the variability when the integration is extended to the western margin. The increased variability away from the western boundary is mainly due to the meandering of the boundary currents and the passage of eddies. A zonal shift of the western boundary current leaves an imprint in the cumulative transport but is not seen in the basinwide zonal integral unless the flow moves toward/away from a sloping margin in which case the external mode projecting onto the MOC can be affected due to upward/downward displacements of the flow. The large variability close to the western margin is consistent with previous modeling (e.g., Böning et al. 1991) and observational (e.g., Bryden et al. 2005b) studies that indicate large fluctuations in the western boundary current system.

Next, ψ_c is split into subannual, seasonal, and interannual components and is illustrated as Hovmöller diagrams for the depth of 1100 m where the thermal wind component ψ_{tw} and the MOC reach their maximum values (Figs. 5–7). The values shown result from a ver-

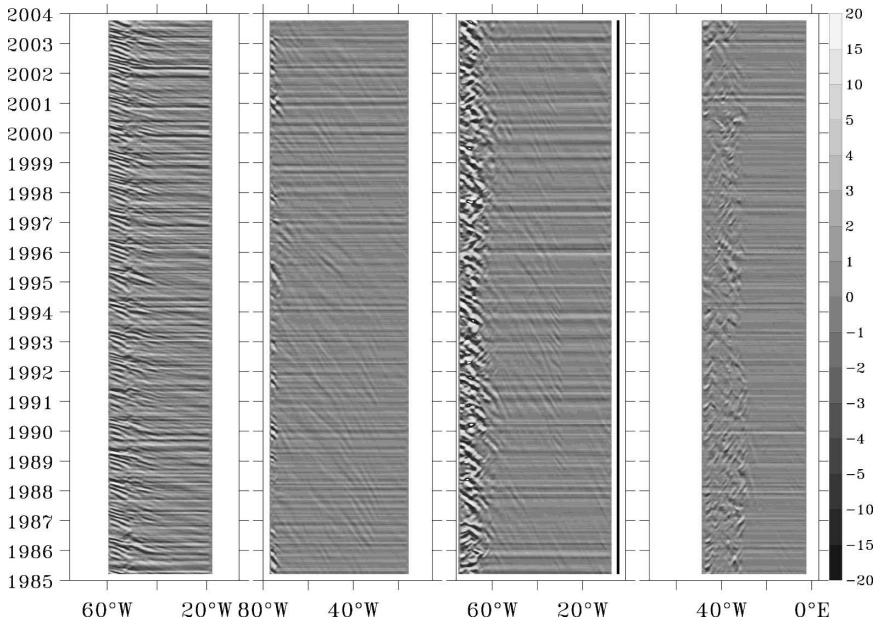

FIG. 5. Hovmöller diagrams for the subannual variability found in the cumulative baroclinic transport ψ_c integrated from the surface to 1100 m (Sv). (from left to right) Latitudes: 10°, 26°, 36°, and 45°N. The contour interval is 1 Sv between values of −5 and 5 Sv and 5 Sv for values outside that range.

tical integration of ψ_c from the surface to 1100 m. Except for 10°N the subannual variability (Fig. 5) is mostly confined to a band of longitudes adjacent to the western boundary. At 10°N the subannual variability shows fluctuations of more than 10 Sv. Even though these are mostly concentrated in the western third of the basin, zonal "stripes" that often start at, or close to, the eastern margin indicate variability farther east (e.g., in 1989, Fig. 5). West of 40°W there is some indication of westward propagation, but the signal is not clear. At

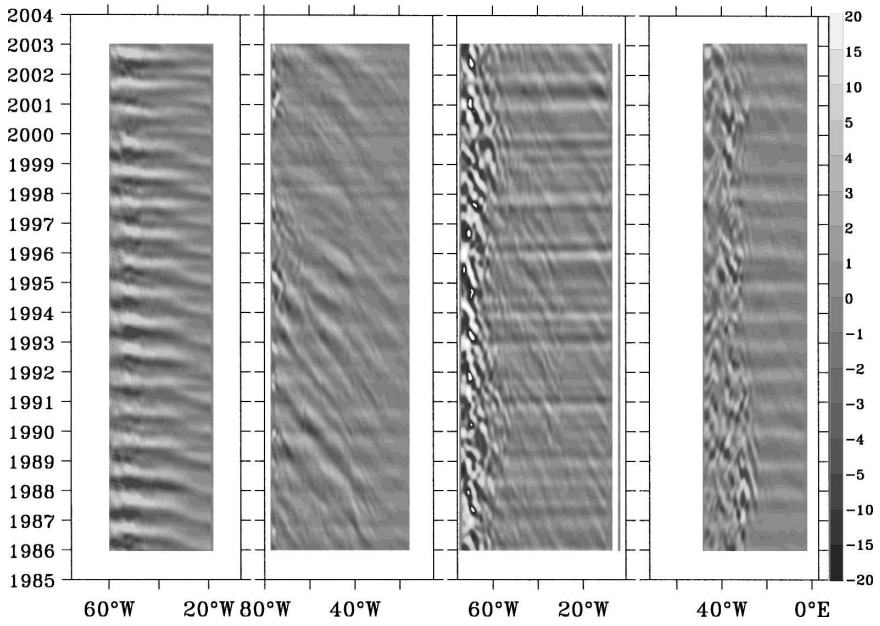

FIG. 6. As in Fig. 5 but for seasonal variability.

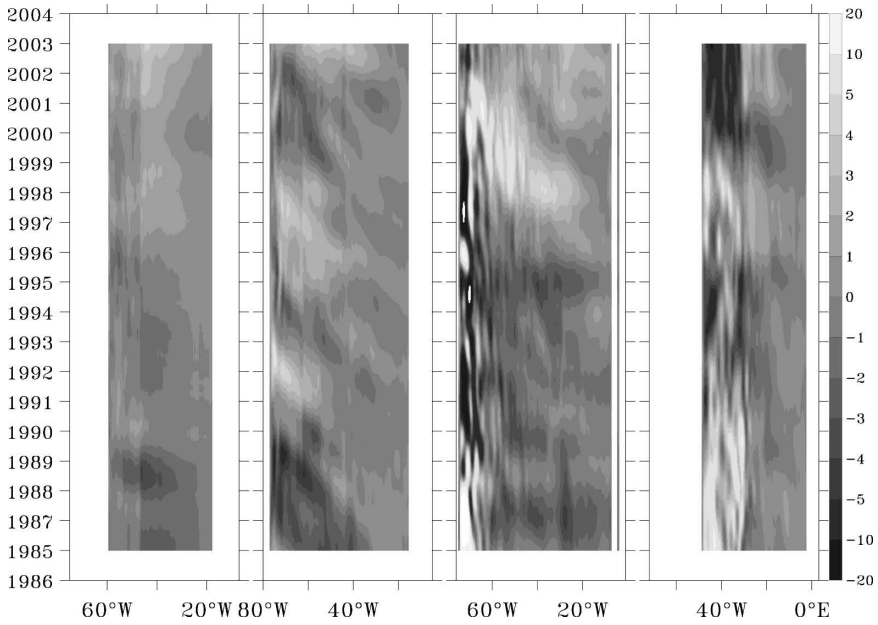

FIG. 7. As in Fig. 5 but for interannual variability.

26°N the subannual signal is weaker than at 10°N but still reaches values up to 8 Sv at the western boundary. Small fluctuations of less than 1 Sv characterize longitudes east of 75°W. Except for a few "ripples" in the basin interior no propagation pattern emerges. At 36°N the anomalies are larger (up to 20 Sv) and mostly confined west of 60°W. A stripy structure characterizes the smaller anomalies (values of up to 2 Sv) found farther east. The same picture is seen at 45°N but with smaller anomalies. Apart from the fact that the largest anomalies related to the subannual variability mainly occur close to the western boundary, zonal stripes of almost constant anomaly values characterize all latitudes. This indicates that some of the subannual variability is generated at the eastern boundary. An anomaly generated at the eastern boundary is seen across the entire basin, provided that no anomaly of opposite sign is encountered during the zonal integration.

On a seasonal time scale substantial anomalies can be found over a large fraction of the basin (Fig. 6). At 10°N near the western boundary the first half of each year is characterized by negative values, whereas positive values are typical for the second half of each year. The anomalies now stretch well into the eastern half of the basin. The signals originate from the eastern margin from where they propagate westward up to a longitude of 30°W. At 30°W the signal amplitude and the westward propagation speed both increase. The signals propagate from 30°W to the western boundary in a few months and the times when they reach the western wall coincide with the times when maximum and minimum values are found for the thermal wind contribution and the MOC. At 26°N the anomalies propagate from east to west and are amplified as they pass 40°W. Unlike at 10°N, where the anomaly pattern is the same each year, at 26°N some anomalies can be tracked for several years over a large fraction of the total basin width, whereas others are short lived. In general, the anomalies undergo several phases of growth and decay as they travel across the basin. An anomaly signal takes about 5 yr to cross the entire basin.

At 36° and 45°N the largest anomalies are confined close to the western boundary, and the basin interior is characterized by zonal anomalies to which no east–west propagation speed can be associated. At 36°N there are some indications of westward propagating signals that take about 5–7 yr to cross the basin, but the picture is not as clear at 26° or 10°N.

No westward propagating signals can be identified at 45°N: the zonal stripes dominating the eastern half of the basin indicate variability originating from the eastern boundary and the anomalies found in the western half of the basin do not exhibit any coherent pattern. This is consistent with the finding of Killworth and Blundell (2003b, 2005), whose ray trajectories show that waves do not propagate far at this latitude.

For the interannual variability (Fig. 7) a westward propagation can be seen for the anomalies at 26° and 36°N, but the picture is less clear than for the seasonal signal. Because these anomalies are much broader than the seasonal ones, it is more difficult to estimate the westward propagation speed, but generally the signals

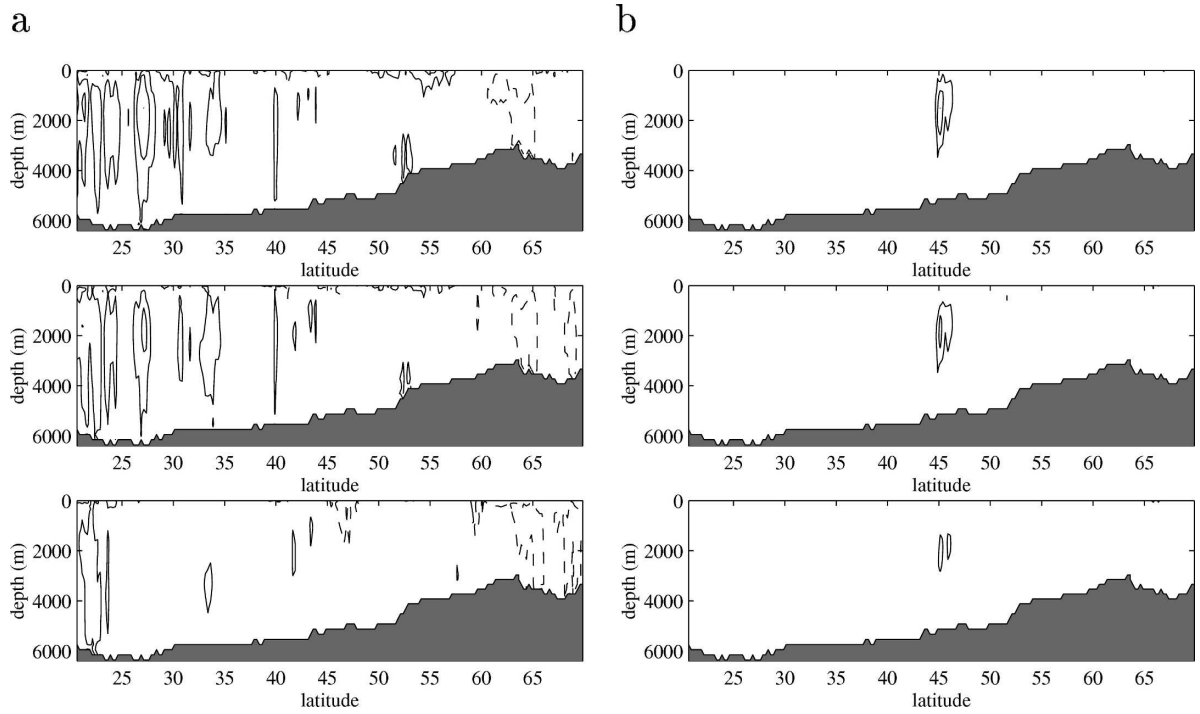

FIG. 8. Lag correlations between the thermal wind contribution ψ_{tw} at 26°N, 1000-m depth and the values of the thermal wind contribution at all other latitudes and depths. (a) Lags are (top) 0, (middle) −1, and (bottom) −2 months, and $\psi_{tw}(y)$, $0° \le y \le 70°$N leads ψ_{tw} ($y = 26°$N); (b) as in (a) but for 45°N and ψ_{tw} (y), $0° \le y \le 70°$N leads ψ_{tw} ($y = 45°$N). Only values larger or smaller than 0.5 and −0.5 are contoured; contour interval is 0.25.

take around 5 years to cross the basin. No difference can be seen between the propagation speeds at 26° and 36°N. At 10° and 45°N no propagation patterns emerge.

Especially on seasonal time scales the latitudes of 10°, 26°, and 36°N exhibit westward propagating features. This signal becomes clearer by removing the zonal mean of the values depicted in Fig. 6. The resulting propagation patterns (not shown) can be associated with Rossby wave activity. The westward velocities for the propagating features seen at 10°, 26°, and 36°N are 20, 4, and 3 cm s^{-1}, respectively. These values are similar to the phase speeds expected for the first baroclinic mode of Rossby waves at these latitudes (e.g., Gill 1982; Killworth and Blundell 2003a). In the results shown in Fig. 6 the Rossby signal is partially masked by other anomalies, especially at 10°N where an even faster signal (30–40 cm s^{-1}) is seen between 30°W and the western boundary. The mechanisms by which the seasonal anomalies are generated are not fully understood, but they could be linked to the wind stress. As shown by Sturges and Hong (1995) fluctuations of the thermocline at 32°N are linked to the wind stress, and the spectrum of the wind curl reveals a maximum at a 12-month period with values gradually increasing from east to west. These results suggest that the wind stress is likely to contribute to the westward amplification of the transport anomalies seen in our study.

d. Origin of thermal wind fluctuations

The results illustrated in Figs. 5–7 indicate that the variability in the thermal wind contribution involves changes over the entire basin width. For the interannual variability the time scale is long enough to allow a first adjustment phase of an ocean basin (e.g., Döscher et al. 1994). However, it is less clear what causes the variability on shorter time scales. Johnson and Marshall (2002) suggest that perturbations traveling from high northern latitudes to the equator as boundary-trapped Kelvin waves along the western boundary, as well as short and long Rossby waves, can modify the strength of the MOC on a seasonal time scale. There are indications that this mechanism is not responsible for the main seasonal signal seen in our study. A lag correlation between the seasonal signal for ψ_{tw} at given latitudes (26° and 45°N) and the signal at the other latitudes of the ocean basin does not indicate a northern origin of the seasonal variability that is consistent with a southward propagating Kelvin wave (Fig. 8). A seasonal variability signal that travels southward as a Kelvin wave should be reflected as a center of maxi-

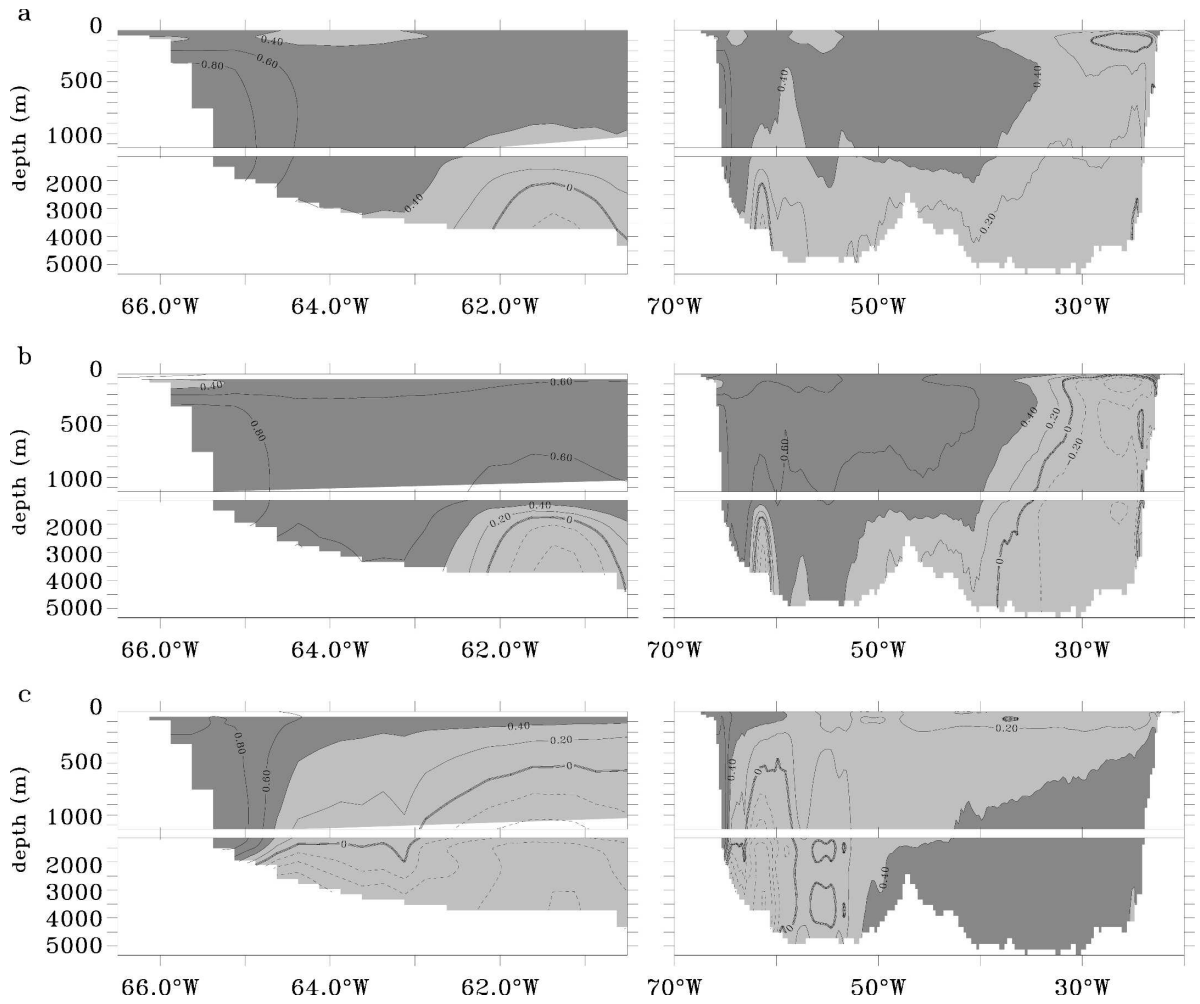

FIG. 9. Correlations between the thermal wind contribution ψ_{tw} at 10°N, 1100-m depth and the cumulative baroclinic transport ψ_c for the (a) subannual, (b) seasonal, and (c) interannual variability; left panels show a zoom on the western boundary. Correlations larger than 0.1 are significant at a confidence level of 0.1%. Contour interval is 0.2; dark gray shading indicates values larger than 0.4.

mum correlation that gradually moves northward as the lag is increased. However, this northward shift is seen neither for 26° (Fig. 8a) nor for 45°N (Fig. 8b). At 26° and 45°N there is little spatial coherence. Shifting a few degrees north or south results in a significant drop in the correlation values. This indicates that the seasonal variability found for the thermal wind contribution at 26° or 45°N is not representative of the behavior of ψ_{tw} over the entire North Atlantic. It also implies that the seasonal signal is likely to be locally generated rather than as a consequence of processes at other latitudes.

Note that this does not exclude the presence of Kelvin waves at the western margin. The total seasonal signal is a combination of variability found at the eastern and western boundaries. The western contribution might contain a Kelvin signal that becomes visible if one only considers transports at the western boundary.

To describe to what extent the variability signals originating from different longitudes contribute to the total changes seen for ψ_{tw} we look at the correlation between the variability found for ψ_{tw} at 1100-m depth and the cumulative transport ψ_c. Figures 9–12 show this correlation for subannual, seasonal, and interannual time scales at 10°, 26°, 36°, and 45°N. At 10°N the variability originating from the eastern boundary does not reflect the fluctuations of ψ_{tw}. Especially for the subannual and seasonal time scales low correlations are found close to the eastern margin (Figs. 9a,b). For the subannual and seasonal signals a substantial fraction of the total variability has its origin between 30° and 40°W where the correlation increases to 0.5 and 0.6. The highest values of more than 0.9 are reached when the zonal integration for ψ_c is extended all the way to the western margin, indicating that a substantial fraction of the total

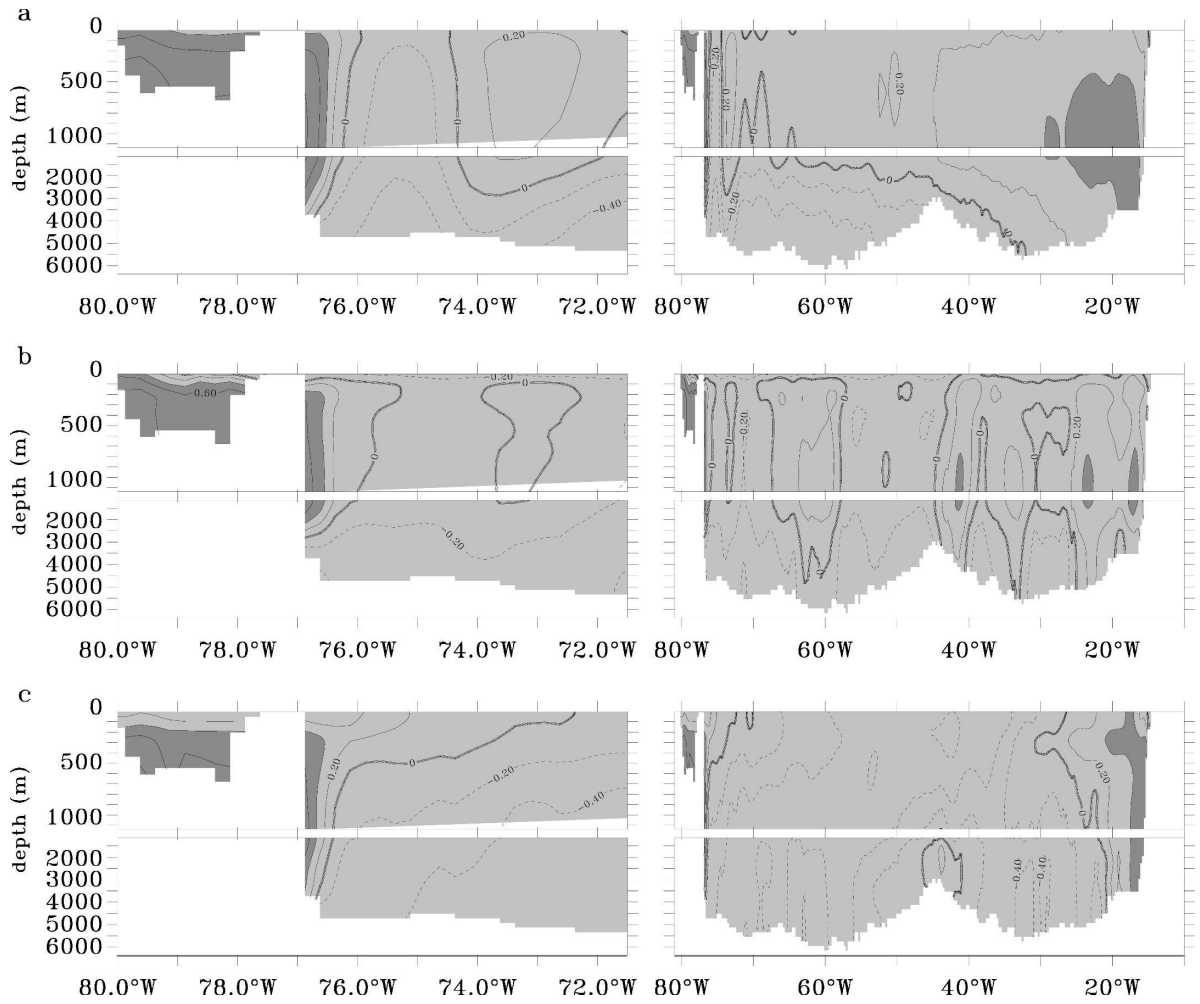

FIG. 10. As in Fig. 9 but at 26°N.

variability is found close to the western boundary (Figs. 9a,b, left panels). Note that the correlation coefficient does not exactly reach 1 at the western boundary unless the margin is vertical from the surface down to at least 1100 m. For sloping sidewalls ψ_c misses a small fraction of the flow because the zonal integration only reaches to the longitude of the margin at a given depth. For the interannual signal there is a higher correlation between the variability at the eastern wall and ψ_{tw}, denoting that on longer time scales the eastern boundary contributes to changes of ψ_{tw} (Fig. 9c). Note that the correlation gradually decreases as the zonal integration for ψ_c is extended westward and an anticorrelation of -0.7 is found at 61°W. It is only in the westernmost longitudes between 61° and 66°W that the correlation value increases to more than 0.9.

At 26°N correlation values between 0.4 and 0.5 are found close to the eastern margin for all three time scales (Fig. 10). For the subannual signal the correlation gradually decreases westward before it increases to 0.8 at the western wall (Fig. 10a). The correlation for the seasonal signal is characterized by local maxima and minima with an increase of the values close to the western margin (Fig. 10b). For the interannual signal extending the integration westward leads to a change in sign, and for a depth of 1000 m a correlation coefficient of about -0.6 is reached at 64°W. As for the subannual and seasonal signals the correlation coefficient increases to 0.7 when the zonal integration is extended to the western wall (Fig. 10c). On all time scales, the variability is partly due to fluctuations in the Straits of Florida where the correlation increases to values of up to 0.9 as the zonal integration is carried across the straits. Note that in OCCAM the fluctuations related to the Straits of Florida are likely to be underestimated since the simulated Florida Current only transports about 15 Sv and exhibits a smaller variability when compared with cable measurements (Baringer and Larsen 2001).

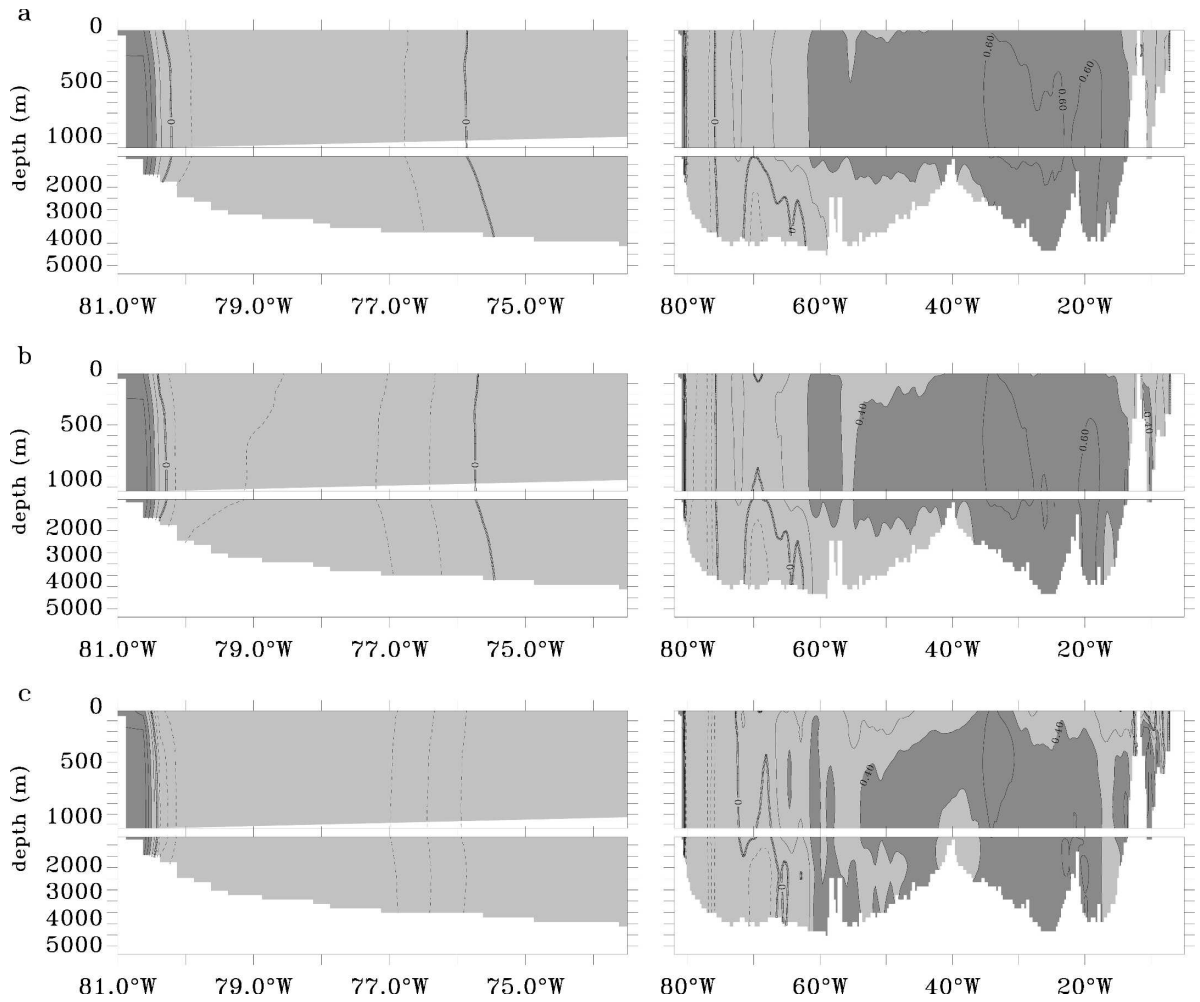

FIG. 11. As in Fig. 9 but at 36°N.

At 36°N values of 0.5–0.6 are found close to the eastern boundary for the variability on all three time scales (Figs. 11a,b). These high correlations remain relatively constant over much of the basin width. Between 60° and 70°W the positive correlations change to an anticorrelation between ψ_{tw} and ψ_c. With values of -0.4, -0.5, and -0.7 for the subannual, seasonal, and interannual variability, respectively, the anticorrelation becomes more pronounced as longer time scales are considered. The final increase to values of more than 0.9 occurs in less than 1° of longitude, indicating that the western margin leaves a clear imprint on the total variability.

At 45°N only little variability originates from longitudes close to the eastern wall and the correlation values are less than 0.4 over much of the section (Fig. 12). As at 26°N, zonal bands of higher values alternate with lower values. High correlations are only reached on the western boundary, indicating that at 45°N most of the variability signal is likely to originate from the western boundary area.

For the interannual variability at 10°, 26°, and 36°N there is an anticorrelation between the cumulative transport ψ_c in the top 1000 m of the ocean east of the western boundary area and the variability in the thermal wind contribution ψ_{tw} to the MOC. In other words, a strengthening of ψ_{tw} coincides with a weakening of the flow in the top 1000 m over a large part of basin. This is consistent with the idea put forward by Bryden et al. (2005a) who suggest that a weakening of the MOC coincides with a strengthening of the horizontal gyre circulation. This feature is not seen, or is at least less pronounced, for the subannual and seasonal variability where there is only little correlation or anticorrelation between the cumulative transport in the top 1100 m east of the western boundary area and the variability of the total transport ψ_{tw}. The results indicate that in order to capture the variability found in the thermal wind

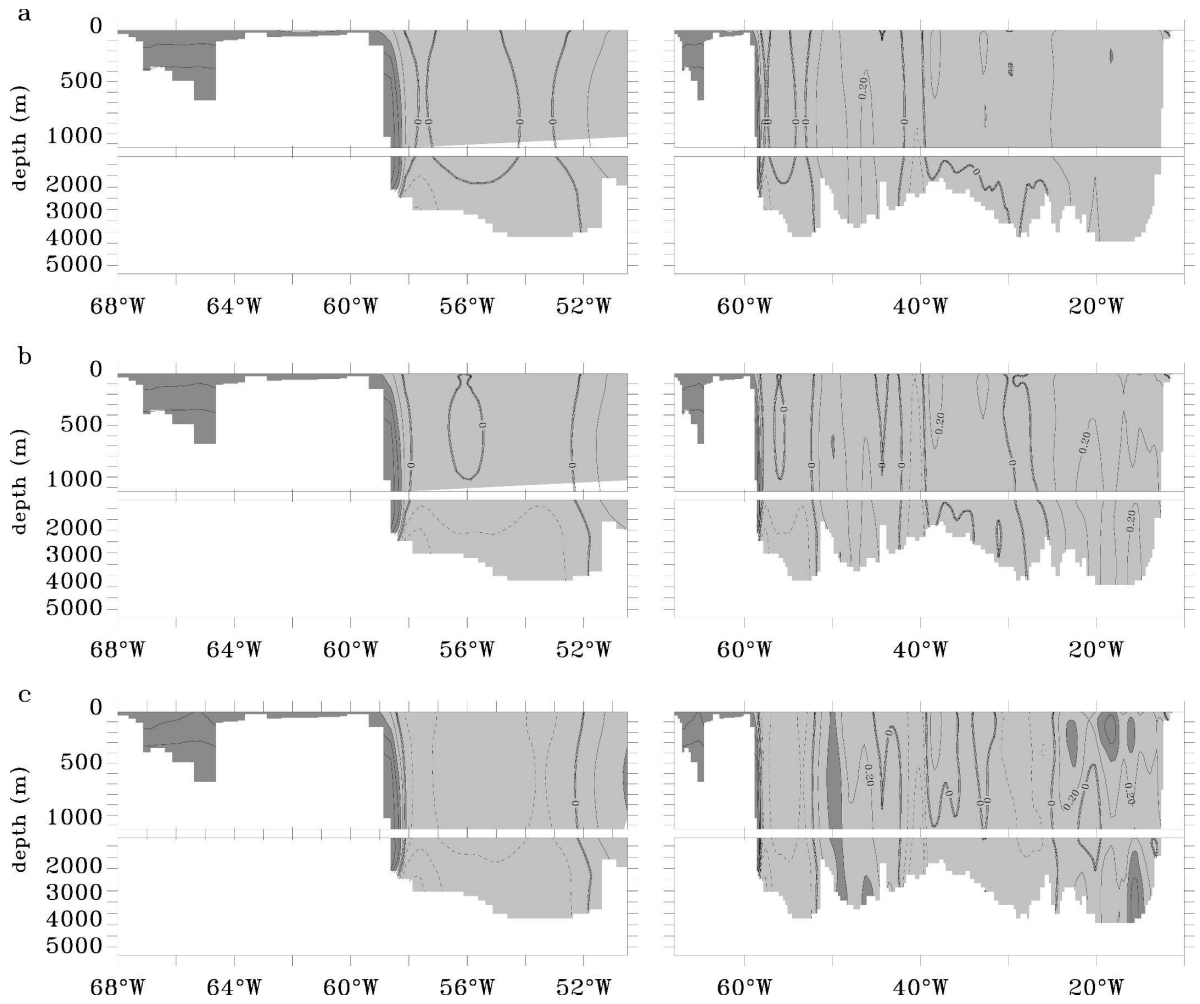

FIG. 12. As Fig. 9 but at 45°N.

contribution ψ_{tw} the entire cumulative transport ψ_c between the eastern and western margins is required. Leaving out even a small fraction of the basin at the eastern or western margin can substantially change the results and lead to a variability signal that is not representative of the entire longitude–depth section.

5. Conceptual model for baroclinic variability

The overall variability found in the thermal wind contribution ψ_{tw} is a function of density perturbations at the eastern and western boundaries. We have shown that these perturbations can have their origin not only at the boundaries, but also in the basin interior, from where they travel westward as baroclinic Rossby waves. Here we present a conceptual picture based on Rossby wave theory in order to assess the size of Rossby wave contributions to fluctuations in the thermal wind component ψ_{tw} of the MOC.

To estimate the size of the changes the basic MOC calculation is revisited. From the thermal wind relation (4) and integrating from west to east (the depth and width are assumed constant for simplicity),

$$f\int v_z\,dx = -g\frac{\Delta\rho}{\rho^*},$$

where $\Delta\rho$ is the east–west density difference. An approximation to the MOC calculations using CTD data is to integrate up from a presumed level of no motion at the floor to give

$$f\int dx\int_{-H}^{z} v_z\,dz \approx -g\int_{-H}^{z}\frac{\Delta\rho}{\rho^*}\,dz,$$

which is corrected by the subtraction of a spatially uniform northward velocity to give no net barotropic transport across the basin. (The actual calculation uses

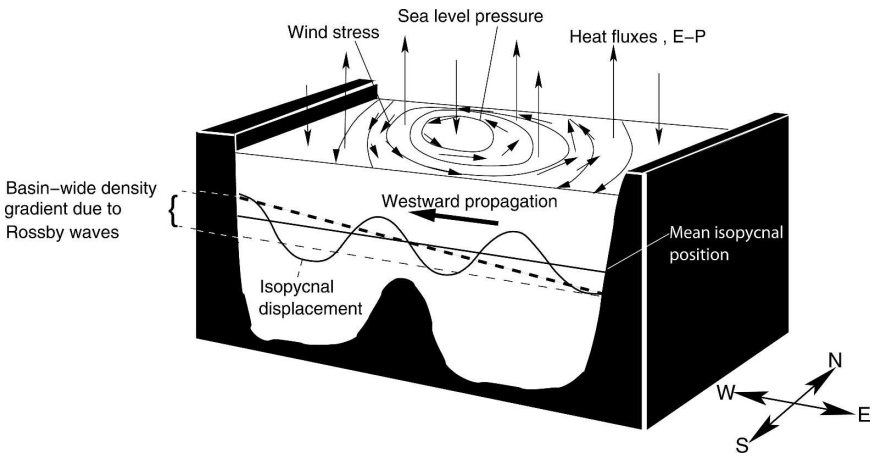

FIG. 13. Schematic for Rossby wave–induced variability of the MOC.

two different levels of no motion, but the simplification here permits useful analysis.)

Suppose a planetary wave signal is present at one or both of the eastern and western boundaries throughout the depth. This causes a perturbation of the density field on the boundaries and, so, adjusts the thermal wind calculation (Fig. 13 gives a schematic). The theory for such waves in the presence of mean flow and topography is discussed in a series of papers by Killworth and Blundell. We assume the waves to be long compared with the deformation radius, in agreement with remotely sensed data, so that the theory of Killworth and Blundell (2003a,b) applies. If the Welander (1959) M function is defined, where M_z = pressure/ρ^*, then in a slowly varying formulation, we write

$$M = F(z; \lambda, \theta) \exp i(k\lambda + l\theta - \omega t)$$

with respect to longitude λ and latitude θ (so that the wavenumbers k, l are dimensionless); ω is the wave frequency. We further assume that the north–south wavenumber l is zero [Killworth and Blundell (2007) show that this makes little difference to the results].[1] The vertical structure F, which is proportional to the vertical velocity, satisfies

$$L(F) \equiv \left(\frac{F_z}{R}\right)_z + \frac{S}{R^2} F = 0, \tag{10}$$

where

$$S = \frac{kN^2}{a^2 f \sin\theta}$$

is proportional to the local stratification N^2 and a is the radius of the earth. The quantity R is minus the local Doppler-shifted frequency (which varies with depth),

$$R = \frac{k\bar{u}}{a\cos\theta} - \omega.$$

Assuming $F(0) = 0$ and no normal flow at the bottom (sloping in general), the eigenvalue problem (10) can be solved for a given frequency to find a small and finite number of wavenumbers k. (The problem is actually one for the phase speed $\omega a \cos\theta/k$, as only the ratio ω/k enters the calculation.) In the following we use the fastest of these modes, whose propagation speeds are known to fit those inferred from altimetry (Killworth and Blundell 2005). The eigenfunction F is scaled by requiring agreement with observations of rms surface elevation η, by

$$F_z(0) = g\eta. \tag{11}$$

A conservative, but typical, value of η = 5 cm is assumed; the results scale linearly with this value.

A Rossby wave of the above form at the western margin results in a perturbation to the standard calculation of the form,

$$f \int dx \int_{-H}^{z} \delta v_z \, dz = +g \int_{-H}^{z} \frac{\delta\rho}{\rho^*} dz, \tag{12}$$

where the prefix δ implies a change from the mean quantity, caused by the perturbation. A wave present on the eastern side produces a similar estimate with a sign change. From the definition of M,

$$F_{zz} = -g\frac{\delta\rho}{\rho^*}$$

so that

[1] Note that the local northward velocity involves knowledge of k (by geostrophy), but does not enter the calculation for the change in MOC.

$$\int dx \int_{-H}^{z} \delta v_z \, dz = -\frac{1}{f}[F_z - F_z(-H)]. \quad (13)$$

Vertical integration generates δv itself, and a possible constant of integration must be determined. Three interpretations δMOC, δMOC′, and δMOC″ are considered since there is no completely consistent way to reproduce the in situ integration across the basin assumed by Hirschi and Marotzke (2007).

The first interpretation assumes that δv remains small near the bottom; the calculation of Hirschi and Marotzke (2007) implicitly assumes this to be the case. The change in the MOC at some depth $z_{\rm ref}$ (taken here as 1100 m, approximately the depth of maximum MOC) is given by

$$\delta\text{MOC} = \int dx \int_{-H}^{z_{\rm ref}} dz \int_{-H}^{z} \delta v_z(z') \, dz'$$

$$= -\frac{1}{f}[F(z_{\rm ref}) - F(-H) - (z_{\rm ref} + H)F_z(-H)]. \quad (14)$$

The second interpretation uses the fact that δv is proportional to F_z by geostrophy (F_z being the pressure), so does not become small at the bottom. Simple integration from $-H$ to $z_{\rm ref}$ of δv then gives an alternative form:

$$\delta\text{MOC}' = -\frac{1}{f}[F(z_{\rm ref}) - F(-H)].$$

Last, we require that there is no net north–south flow produced by either the west or east component of the perturbation (though there is no reason that these should be coherent across the basin). Then we write (13) as

$$\int dx \, (\delta v - \delta v_b) = \int dx \int_{-H}^{z} \delta v_z \, dz$$

$$= -\frac{1}{f}[F_z - F_z(-H)], \quad (15)$$

where $\delta v_b = \delta v(-H)$, and require that

$$\int dx \int_{-H}^{0} dz \, \delta v = 0$$

so that

$$-H \int dx \, \delta v_b = -\frac{1}{f}[F(0) - F(-H) - HF_z(-H)]. \quad (16)$$

Then, since $F(0)$ vanishes,

$$\delta\text{MOC}'' = -\frac{1}{f}\left[F(z_{\rm ref}) + \frac{z_{\rm ref}}{H}F(-H)\right], \quad (17)$$

and we shall quote the values of all three possible formulations for comparison. For a flat bottom, the condition of no normal flow implies $F(-H) = 0$ so that δMOC′ = δMOC″.

The full change to the MOC involves both west and east boundaries. It is likely that the wave processes at the two boundaries are incoherent, that there is no available data connecting the phases at the eastern and western margins, and that surface forcing of waves during their propagation serves to destroy the phase information. So, writing

$$\delta\text{MOC(full)} = \delta\text{MOC(west)} \exp(i\phi_{\rm west}) + \delta\text{MOC(east)} \exp(i\phi_{\rm east}),$$

where the ϕ are unknown phases, then

$$\text{rms}[\delta\text{MOC(full)}] = \frac{1}{2^{1/2}}[\delta\text{MOC(west)}^2 + \delta\text{MOC(east)}^2]^{1/2}$$

can be used to estimate the amplitude of the combined eastern and western contributions.[2]

The size of the expected value of δMOC can be estimated by considering the simplest model in which the buoyancy frequency is constant, there is no mean flow, and the bottom is flat. The (lowest internal mode) perturbation solution is $F = (g\eta H/\pi) \sin[\pi(z + H)/H]$, giving

$$\delta\text{MOC} = -\frac{g\eta H}{\pi f}\left[\sin\frac{\pi(z_{\rm ref} + H)}{H} - \frac{\pi(z_{\rm ref} + H)}{H}\right] \quad \text{and}$$

$$\delta\text{MOC}' = \delta\text{MOC}'' = -\frac{g\eta H}{\pi f}\sin\frac{\pi(z_{\rm ref} + H)}{H},$$

both of whose magnitudes are $O(g\eta H/\pi f)$, which is about 6 Sv. Plots of the absolute value of these quantities (Sv) for $H = 4000$ m are shown in Fig. 14 as a function of latitude. The rms value would be $2^{1/2}$ times this.

The reliability of this simple estimate depends on the density structure and flow profiles. For any more complete problem, data processing follows the approach of Killworth and Blundell (2003a,b) to obtain solutions for

[2] If more than two stations are used to estimate the MOC (Baehr et al. 2004), then the effects of wave activity at stations intermediate between west and east will tend to cancel, by geostrophy, apart from the smaller effects of differing depths H at different stations.

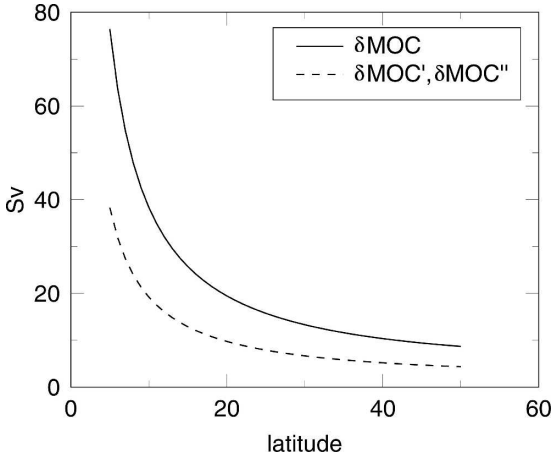

FIG. 14. Components of the change to the MOC (for three possible interpretations) for constant buoyancy frequency, no flow, and uniform depth at z_{ref} = 1100 m.

F at any given location. The positions of "west" and "east" are found by specifying a target depth, and for each latitude using the 1° × 1° average of the 5-minute global bathymetry and topography dataset ETOPO5 (National Geophysical Data Center 1988) to locate the point respectively farthest west or east of the Mid-Atlantic Ridge with a depth at least the target depth. The density field is computed from the *World Ocean Atlas* dataset (Antonov et al. 1998a,b,c; Boyer et al. 1998a,b,c). In some cases near steep topography, solutions cannot be found because the thermal wind shear cannot be reliably estimated down to the bottom; in other cases there may simply be no eigensolution.

Figure 15 shows the equivalent of Fig. 14, but using the in situ buoyancy frequency (retaining no flow and a bottom depth of 4000 m, taken to be locally flat), as well as the rms estimate of the full signal. While the δMOC′ signal remains O(5 Sv), the δMOC signal drops to O(2) Sv over much of the latitude range.

Figure 16 shows the δMOC values as a function of latitude, again for a depth of 4000 m, when mean flow and bottom slope are both included. The mean flow is calculated from the density by thermal wind and then adjusted so as to be purely baroclinic. It is clear that the three definitions often give radically different estimates, both in magnitude and sign (since the phase, and by implication the time scale, is unknown, the sign is only relevant when comparing the δMOC and δMOC′ estimates with each other). Near the equator, large values are found due to the division by a small f. As noted, there are some missing values where solutions propagating solely along lines of latitude cannot be found.

The combination of west and east yields the rms values in Fig. 17. This shows that almost everywhere variations of a few Sverdrups are to be expected from the existence of realistic Rossby waves.

The contribution of δMOC″ corresponds most closely to the calculation of ψ_{tw} in OCCAM [Eq. (3)], and can therefore be compared with the variability found for ψ_{tw}. The combined contributions from $\delta MOC''_w$ and $\delta MOC''_e$ suggest that for most latitudes between 5° and 50°N the Rossby wave activity can be linked to MOC contributions of several Sverdrups (Fig. 18). Since $\delta MOC''_w$ and $\delta MOC''_e$ are representative of maximum contributions, the values shown in Fig. 18 are generally higher (1–7 Sv) than the standard deviation found for ψ_{tw} (0.5–4 Sv, Fig. 2b). It is interesting to note that the

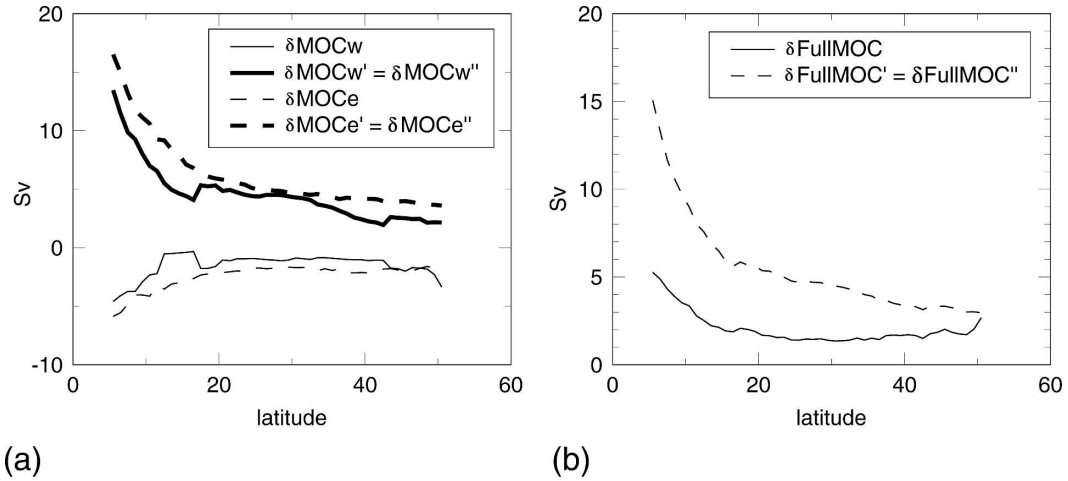

FIG. 15. (a) Contributions to the western and eastern changes to the MOC using in situ buoyancy frequency, no flow, and a flat bottom as a function of latitude. (b) Standard deviation of the expected full contribution to MOC changes from both sides of the ocean. Both are computed at the depth z_{ref} = 1100 m.

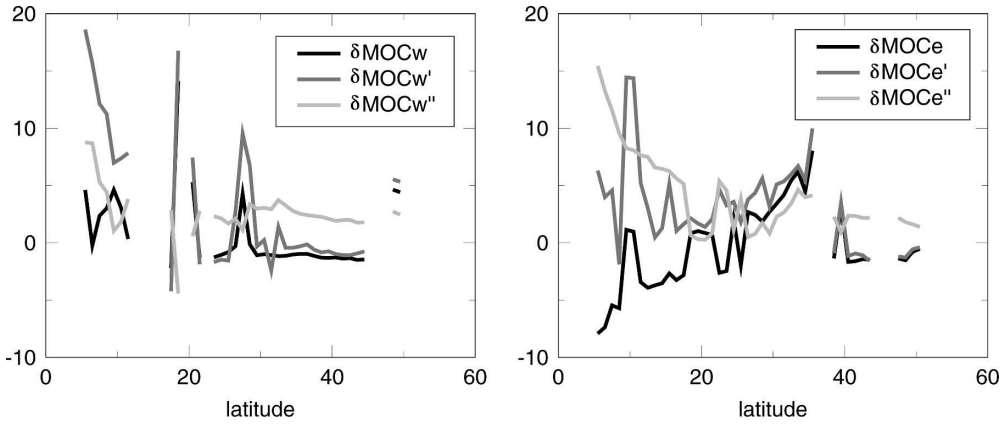

FIG. 16. As in Fig. 15a but using the baroclinic mean flow at west and east sides of the Atlantic and a sloping bottom. Gaps show where solutions could not be found. The solutions are computed at the depth $z_{\text{ref}} = 1100$ m.

vertical structure of the fluctuations depicted in Fig. 2b and Fig. 18 is similar. In both cases the maximum variability is found close to the 1100-m value assumed for z_{ref} on the basis of the circulation simulated in OCCAM. This suggests that the conceptual picture based on fluctuations of the first baroclinic mode is consistent with the variability found in the eddy-permitting model for ψ_{tw}.

Changing the ocean depth to 4500 m, say, (not shown) has small quantitative but not qualitative effects on the solutions. In summary, we conclude that the ubiquity of planetary waves can cause variations in the value of the MOC by $O(3–4)$ Sv.

6. Discussion

One question that has not been fully addressed yet is what causes the anomalies in the density field that lead to changes in the thermal wind contribution. For changes originating from the eastern boundary, such as those seen at 26° and 36°N, a plausible mechanism has been suggested by Köhl (2005) who argues that wind-driven downwelling and upwelling close to the eastern boundary can disturb the isopycnal structure and therefore the basinwide east–west density gradient. Developing this idea further, it is conceivable that such changes propagate westward as Rossby waves. In this study a clear indication of Rossby wave activity can be found at 10°, 26°, and 36°N (Fig. 6). The wave signals generally undergo several phases of growth and decay as they travel across the basin. Sometimes the wave signal disappears and other times it amplifies as it propagates westward, allowing it to reach the western wall where it affects the basinwide density difference. The waves do not have to originate from the eastern margin itself. It is conceivable that the combined activity of the surface forcing (wind, heat, $E - P$, sea level pressure fluctuations) or baroclinic instabilities generate Rossby waves in the basin interior as well. This would be consistent with Killworth and Blundell (2007) or with Sturges and Hong (1995) who show a link between changes of the thermocline and the wind stress at 32°N. The amplification of anomalies seen for the cumulative transport at certain longitudes (e.g., 30°W at 10°N or between 40° and 50°W at 26°N, see Fig. 6) is linked to a variability in the isopycnal slope at those longitudes. However, it has to be said that, apart from 10°N where the anomalies in the cumulative transport ψ_c can clearly be linked to the changes in the zonal and meridional wind stress, the exact mechanisms are diffi-

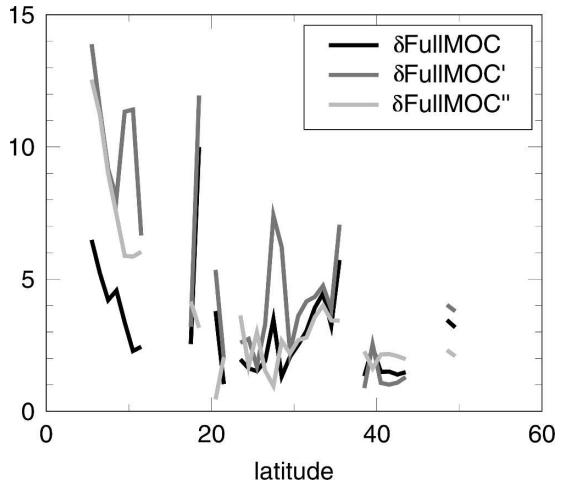

FIG. 17. As in Fig. 15b but using the baroclinic mean flow at west and east sides of the Atlantic and a sloping bottom. Gaps show where solutions could not be found. The solutions are computed at the depth $z_{\text{ref}} = 1100$ m. Units: Sv.

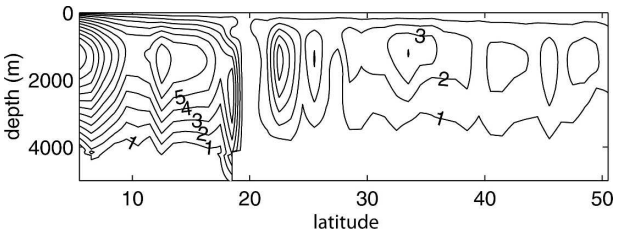

FIG. 18. MOC contribution $\delta MOC''$. Where solutions are defined for $\delta MOC''_w$ and $\delta MOC''_e$ the contoured values represent the rms. If no solution can be found at either the eastern or western margin, we plot the absolute values of $\delta MOC''_w$ or $\delta MOC''_e$ respectively. Units: Sv; contour interval is 1 Sv.

cult to pinpoint for 26°, 36°, and 45°N. At the western boundary the density structure is likely to be affected by Kelvin and short Rossby waves as well. The fact we do not see transport anomalies propagating equatorward does not mean that the mechanisms described in Johnson and Marshall (2002) do not occur in our model. Southward propagating signals are very hard to detect because of anomalies generated at all latitudes by the surface forcing. In our study the locally generated anomalies are large enough to blur any clear boundary-trapped signal traveling equatorward.

The approach used in our conceptual theoretical model to calculate MOC anomalies is the same as that commonly used for observational data (hydrographic sections or mooring data). In both cases the meridional transport is calculated from zonal density differences. The theoretical results are a first step in understanding the large variability found on short time scales for the thermal wind (baroclinic) contribution in the numerical model. This large variability is one of the difficulties one might encounter when interpreting real ocean data. One of the major aims of MOC studies based either on hydrographic sections or on observing systems, such as those deployed in the RAPID framework, is to provide reliable information about the current state of the MOC and maybe, even more importantly, to assess whether the MOC is undergoing a major rearrangement. The results shown in this paper indicate that significant fluctuations of the MOC can occur on very short time scales. However, these fluctuations are short lived and are not representative for a long-term trend that is of climatic relevance. As the theoretical results in section 5 show, such short-term fluctuations could be linked to local Rossby wave activity. Such MOC fluctuations also mean that a consistent weakening of the MOC might be masked unless the MOC is monitored over a long period of time (Baehr et al. 2007). However, there might be ways to separate the MOC variability into signals that are relevant to the climate or not. As indicated in section 4d, an anticorrelation can be seen between the variability found for the thermal wind contribution and the cumulative transport east of the western boundary area on interannual time scales. This anticorrelation is not seen or is at least much smaller on the subannual and seasonal time scales. A detailed analysis of this behavior and its robustness is beyond the scope of the present paper, but could be an area worth investigating.

7. Conclusions

Based on our study of the MOC variability on subannual, seasonal, and interannual time scales we conclude the following:

- Both wind stress and variations in the thermal wind contribute to the total variability seen for the MOC. In the numerical model used here the wind stress–related fluctuations are mostly confined to subannual and seasonal time scales, whereas the thermal wind leads to variations on interannual time scales as well.
- Even on subannual and seasonal time scales a large fraction of the MOC variability is due to fluctuations of the density field.
- The perturbations of the density field and the related meridional transport anomalies can have their origin at the western and eastern margins as well as in the basin interior. On seasonal time scales there is only little meridional coherence for the variability found in the thermal wind contribution, thus indicating that it is most likely locally generated rather than a response to high- or low-latitude processes.
- On seasonal (and to a lesser extent subannual) time scales, anomalies of the meridional transport propagate westward with the characteristic phase speed of baroclinic Rossby waves. Clear westward propagating signals are seen for 10°, 26°, and 36°N. No westward propagation can be seen at 45°N.
- A conceptual model based on the assumption that the basinwide meridional transport is modified according to the phase difference between Rossby waves at the eastern and western boundaries suggests that Rossby wave activity could account for short-term (seasonal or shorter) fluctuations of several Sverdrups for the thermal wind contribution to the MOC.
- The presence of large short-term variability for the MOC is likely to affect the interpretation of real ocean data from both hydrographic sections and observing systems such as the ones deployed in the framework of RAPID.

Acknowledgments. We thank Beverly de Cuevas and Andrew Coward for their help with the OCCAM

model. We also thank Harry Bryden and Rémi Tailleux for stimulating discussions and two anonymous reviewers for their useful comments. This work was supported by the Natural Environment Research Council as part of the RAPID program and by the University of Southampton.

REFERENCES

Antonov, J., S. Levitus, T. P. Boyer, M. Conkright, T. O'Brien, and C. Stephens, 1998a: *Temperature of the Atlantic Ocean.* Vol. 1, *World Ocean Atlas 1998,* NOAA Atlas NESDIS 27, 166 pp.

——, ——, ——, ——, ——, and ——, 1998b: *Temperature of the Pacific Ocean.* Vol. 2, *World Ocean Atlas 1998,* NOAA Atlas NESDIS 28, 166 pp.

——, ——, ——, ——, ——, ——, and B. Trotsenko, 1998c: *Temperature of the Indian Ocean.* Vol. 3, *World Ocean Atlas 1998,* NOAA Atlas NESDIS 29, 166 pp.

Baehr, J., J. Hirschi, J.-O. Beismann, and J. Marotzke, 2004: Monitoring the meridional overturning circulation in the North Atlantic: A model-based array design study. *J. Mar. Res.,* **62,** 283–312.

——, K. Keller, and J. Marotzke, 2007: Detecting potential changes in the meridional overturning circulation at 26°N in the Atlantic. *Climatic Change,* in press.

Baringer, M. O., and J. C. Larsen, 2001: Sixteen years of Florida Current transport. *Geophys. Res. Lett.,* **28,** 3179–3182.

Böning, C. W., R. Döscher, and R. G. Budich, 1991: Seasonal transport variation in the western subtropical North Atlantic: Experiments with an eddy-resolving model. *J. Phys. Oceanogr.,* **21,** 1271–1289.

Boyer, T. P., S. Levitus, J. I. Antonov, M. Conkright, T. O'Brien, and C. Stephens, 1998a: *Salinity of the Atlantic Ocean.* Vol. 4, *World Ocean Atlas 1998,* NOAA Atlas NESDIS 30, 166 pp.

——, ——, ——, ——, ——, and ——, 1998b: *Salinity of the Pacific Ocean.* Vol. 5, *World Ocean Atlas 1998,* NOAA Atlas NESDIS 31, 166 pp.

——, ——, ——, ——, ——, ——, and B. Trotsenko, 1998c: *Salinity of the Indian Ocean.* Vol. 6, *World Ocean Atlas 1998,* NOAA Atlas NESDIS 32, 166 pp.

Broecker, W. S., G. Bond, M. Klas, E. Clark, and J. McManus, 1992: Origin of the northern Atlantic's Heinrich events. *Climate Dyn.,* **6,** 265–273.

Bryan, K., 1982: Seasonal variation in meridional overturning and poleward heat transport in the Atlantic and Pacific Oceans: A model study. *J. Mar. Res.,* **40,** 39–53.

Bryden, H. L., H. R. Longworth, and S. A. Cunningham, 2005a: Slowing of the Atlantic meridional overturning circulation at 25°N. *Nature,* **438,** 655–657.

——, W. E. Johns, and P. M. Saunders, 2005b: Deep western boundary current east of Abaco: Mean structure and transport. *J. Mar. Res.,* **63,** 35–57.

Dansgaard, W., and Coauthors, 1993: Evidence for general instability of past climate from a 250-kyr ice-core record. *Nature,* **364,** 218–220.

Delworth, T. L., and R. J. Greatbatch, 2000: Multidecadal thermohaline circulation variability driven by atmospheric surface flux forcing. *J. Climate,* **13,** 1481–1495.

——, S. Manabe, and R. J. Stouffer, 1993: Interdecadal variations of the thermohaline circulation in a coupled ocean–atmosphere model. *J. Climate,* **6,** 1993–2011.

Deshayes, J., and C. Frankignoul, 1995: Spectral characteristics of the response of the meridional overturning circulation to deep-water formation. *J. Phys. Oceanogr.,* **35,** 1813–1825.

Donners, J., and S. S. Drijfhout, 2004: Impact of cooling on the water mass exchange of the Agulhas rings in a high resolution ocean model. *Geophys. Res. Lett.,* **31,** L16312, doi:10.1029/2004GL020644.

Döscher, R. C., C. W. Böning, and P. Herrman, 1994: Response of circulation and heat transport in the North Atlantic to changes in thermohaline forcing in northern latitudes: A model study. *J. Phys. Oceanogr.,* **24,** 2306–2320.

Eden, C., and R. J. Greatbatch, 2003: A damped oscillation in the North Atlantic climate system. *J. Climate,* **16,** 4043–4060.

Ganopolski, A., and S. Rahmstorf, 2001: Rapid changes of glacial climate simulated in a coupled climate model. *Nature,* **409,** 153–158.

Gill, A. E., 1982: *Atmosphere–Ocean Dynamics.* Academic Press, 662 pp.

Heinrich, H., 1988: Origin and consequences of cyclic ice rafting in the northeast Atlantic Ocean during the past 130,000 years. *Quat. Res.,* **29,** 142–152.

Hirschi, J., and J. Marotzke, 2007: Reconstructing the meridional overturning circulation from boundary densities and the zonal wind stress. *J. Phys. Oceanogr.,* **37,** 743–763.

Houghton, J. T., Y. Ding, D. J. Griggs, M. Noguer, P. J. van der Linden, X. Dai, K. Maskell, and C. A. Johnson, Eds., 2001: *Climate Change 2001: The Scientific Basis*. Cambridge University Press, 881 pp.

Jayne, S. R., and J. Marotzke, 2001: The dynamics of ocean heat transport variability. *Rev. Geophys.,* **39,** 385–411.

Johnson, H. L., and D. P. Marshall, 2002: A theory of the surface Atlantic response to thermohaline variability. *J. Phys. Oceanogr.,* **32,** 1121–1132.

Kalnay, E., and Coauthors, 1996: The NCEP/NCAR 40-Year Reanalysis Project. *Bull. Amer. Meteor. Soc.,* **77,** 437–471.

Kawase, M., 1987: Establishment of deep ocean circulation driven by deep-water production. *J. Phys. Oceanogr.,* **17,** 2294–2317.

Killworth, P. D., and J. R. Blundell, 2003a: Long extratropical planetary wave propagation in the presence of slowly varying mean flow and bottom topography. Part I: The local problem. *J. Phys. Oceanogr.,* **33,** 784–801.

——, and ——, 2003b: Long extratropical planetary wave propagation in the presence of slowly varying mean flow and bottom topography. Part II: Ray propagation and comparison with observations. *J. Phys. Oceanogr.,* **33,** 802–821.

——, and ——, 2005: The dispersion relation for planetary waves in the presence of mean flow and topography. Part II: Two-dimensional examples and global results. *J. Phys. Oceanogr.,* **35,** 2110–2133.

——, and ——, 2007: Planetary wave response to surface forcing and to instability in the presence of mean flow and topography. *J. Phys. Oceanogr.,* **37,** 1297–1320.

Köhl, A., 2005: Anomalies of meridional overturning: Mechanisms in the North Atlantic. *J. Phys. Oceanogr.,* **35,** 1455–1472.

Lang, C., M. Leuenberger, J. Schwander, and S. Johnsen, 1999: 16°C rapid temperature variation in central Greenland 70,000 years ago. *Science,* **286,** 934–937.

Levitus, S., and Coauthors, 1998: *Introduction.* Vol. 1, *World Ocean Database 1998,* NOAA Atlas NESDIS 18, 346 pp.

Marotzke, J., and J. Willebrand, 1991: Multiple equilibria of the global thermohaline circulation. *J. Phys. Oceanogr.,* **21,** 1372–1385.

——, S. A. Cunningham, and H. L. Bryden, cited 2002: Monitor-

ing the Atlantic meridional overturning circulation at 26.5°N. [Available online at http://www.noc.soton.ac.uk/rapidmoc.]

Marsh, R., B. A. de Cuevas, A. C. Coward, H. L. Bryden, and M. Alvarez, 2005a: Thermohaline circulation at three key sections in the North Atlantic over 1985–2002. *Geophys. Res. Lett.,* **32,** L10604, doi:10.1029/2004GL022281.

——, ——, ——, A. J. G. Nurser, and S. A. Josey, 2005b: Water mass transformation in the North Atlantic over 1985–2002 simulated in an eddy-permitting model. *Ocean Sci. Discuss.,* **2,** 63–104.

National Geophysical Data Center, 1988: Digital relief of the surface of the Earth. NOAA Data Announcement 88-MGG-O2. [Available online at http://www.ngdc.noaa.gov/mgg/global/etopo5.html.]

Petit, J. R., and Coauthors, 1999: Climate and atmospheric history of the past 420,000 years from the Vostok ice core, Antarctica. *Nature,* **399,** 429–436.

Polyakov, I. V., U. S. Bhatt, H. L. Simmons, D. Walsh, J. E. Walsh, and X. Zhang, 2005: Multidecadal variability of North Atlantic temperature and salinity during the twentieth century. *J. Climate,* **18,** 4562–4580.

Schopf, P. S., 1980: The role of Ekman flow and planetary waves in the oceanic cross-equatorial heat transport. *J. Phys. Oceanogr.,* **10,** 330–341.

Siegenthaler, U., and Coauthors, 2005: Stable carbon cycle–climate relationship during the late Pleistocene. *Science,* **310,** 1313–1317.

Stommel, H., 1961: Thermohaline convection with two stable regimes of flow. *Tellus,* **13,** 224–241.

Sturges, W., and B. G. Hong, 1995: Wind forcing of the Atlantic thermocline along 32°N at low frequencies. *J. Phys. Oceanogr.,* **25,** 1706–1715.

Trenberth, K. E., and J. M. Caron, 2001: Estimates of meridional atmosphere and ocean heat transports. *J. Climate,* **14,** 3433–3443.

Tziperman, E., 1997: Inherently unstable climate behaviour due to weak thermohaline ocean circulation. *Nature,* **386,** 592–595.

Vellinga, M., and R. A. Woods, 2002: Global impacts of a collapse of the Atlantic thermohaline circulation. *Climatic Change,* **54,** 251–267.

Webb, D. J., 1996: An ocean model code for array processor computers. *Comput. Geosci.,* **22,** 569–578.

Welander, P., 1959: An advective model of the ocean thermocline. *Tellus,* **11,** 309–318.

Willebrand, J., G. H. Philander, and R. C. Pacanowski, 1980: The oceanic response to large-scale atmospheric disturbances. *J. Phys. Oceanogr.,* **10,** 411–429.

Zanna, L., and E. Tziperman, 2005: Nonnormal amplification of the thermohaline circulation. *J. Phys. Oceanogr.,* **35,** 1593–1605.